



HAL
open science

Simulation study of an X-ray diffraction system for breast tumor detection

Fanny Marticke, G Montémont, C Paulus, Olivier J.J. Michel, Jerome I. Mars,
L I Verger

► **To cite this version:**

Fanny Marticke, G Montémont, C Paulus, Olivier J.J. Michel, Jerome I. Mars, et al.. Simulation study of an X-ray diffraction system for breast tumor detection. Nuclear Instruments and Methods in Physics Research Section A: Accelerators, Spectrometers, Detectors and Associated Equipment, 2017, 867, pp.20 - 31. 10.1016/j.nima.2017.04.026 . hal-01552429

HAL Id: hal-01552429

<https://hal.science/hal-01552429>

Submitted on 24 Aug 2017

HAL is a multi-disciplinary open access archive for the deposit and dissemination of scientific research documents, whether they are published or not. The documents may come from teaching and research institutions in France or abroad, or from public or private research centers.

L'archive ouverte pluridisciplinaire **HAL**, est destinée au dépôt et à la diffusion de documents scientifiques de niveau recherche, publiés ou non, émanant des établissements d'enseignement et de recherche français ou étrangers, des laboratoires publics ou privés.

1 Simulation study of an X-ray diffraction system for
2 breast tumor detection

3 F. Marticke^{a,b}, G. Montemont^a, C. Paulus^a, O. Michel^b, J. I. Mars^b,
4 L. Verger^a

5 ^a*Univ. Grenoble-Alpes, F-38000 Grenoble, France*

6 *CEA, LETI, Minatec Campus, F-38054 Grenoble, France*

7 ^b*Univ. Grenoble-Alpes, Gipsa-Lab, F-38000 Grenoble, France*

8 *CNRS, Gipsa-Lab, F-38000 Grenoble, France*

9 **Abstract**

10 X-ray diffraction (XRD) is a powerful technique used to determine the molec-
11 ular structure of biological tissues. In breast tissues for example, the scattering
12 signatures of dense fibroglandular tissue and carcinoma have been shown to be
13 significantly different. In this study, XRD was used as a second control level
14 when conventional mammography results were unclear, for instance because of
15 overly high breast density. A system optimized for this issue, called multifocal
16 XRD, was developed combining energy dispersive spectral information at dif-
17 ferent scattering angles. This system allows depth-imaging in one go but needs
18 an x,y-direction scan to image the region conventional mammography identified
19 as suspect. **The scan-time for about 10 cm³ with an incident flux of about**
20 **4.8·10⁷ photons per second would be around 2 seconds.** For this study, breast
21 phantoms with and without cancerous nodule were simulated to assess the sep-
22 aration power of the method and to determine the radiation dose required to
23 obtain nearly ideal separation. For tumors situated in the center of the breast,
24 the required dose was only about 0.3 mGy, even for breasts with high density.
25 The tumor position was shown to have a low impact on detectability provided
26 it remained in a zone where the system was sufficiently sensitive. The influence
27 of incident spectrum maximum energy was also studied. The required dose re-
28 maind very low with any of the incident spectra tested. Finally, an image slice
29 was reconstructed in the x-direction and showed that the system can detect the

30 presence of a small tumor (4 mm). Hence, XRD is a very promising tool to
31 reduce the number of unnecessary invasive breast biopsies.

32 *Keywords:* X-ray scattering, breast cancer, breast phantom simulation,
33 radiation dose, system optimization, depth imaging, reconstruction.

34 1. Introduction

35 Conventional mammography is based on the premise that normal breast
36 tissue and cancerous tissue differ in how they absorb X-rays. Mammography is
37 currently believed to be the most effective breast screening tool. However, it is
38 limited by the low contrast between the details to be detected (e.g. nodules) [1]
39 and the background composed of adipose and fibroglandular tissues. The higher
40 the proportion of fibroglandular tissue (i.e., the more dense the breast tissue),
41 the more difficult it will be to detect a small lesion. This difficulty can lead to
42 false negative or false positive diagnoses, resulting in missed cancer detection or
43 unnecessary biopsies.

44 As breast biopsy is an invasive technique which causes patients considerable
45 stress, the number of unnecessary ones should be reduced. This article proposes
46 a non-invasive X-ray diffraction (XRD) method which could reduce the number
47 of unnecessary breast biopsies. XRD can detect the molecular structure of
48 biological tissues [2] which is not possible with X-ray absorption. Hence, it
49 delivers additional information about the tissue to be classified. The potential
50 of XRD to improve breast cancer diagnosis was recognized by numerous authors.
51 Some of them suggested to enhance contrast of conventional mammography by
52 combining transmission and coherent scattering images [3–5]. XRD as a stand-
53 alone technique was also considered. Different XRD computed tomography
54 systems were proposed [6–9]. The most important problem of XRD in breast
55 cancer diagnosis is the system sensitivity, which implies long measurement time
56 [10–12] and high dose delivery. Chaparian *et al.* [13, 14] proposed a method to
57 optimize an energy dispersive X-ray diffraction system for clinical applications in
58 terms of sensitivity notably. Though, this system only acquires at one scattering

59 angle and acquisition of thicker objects requires a depth scan. Moreover, their
60 study did not include dose considerations. Ghammraoui *et al.* [15, 16] analyzed
61 the impact of delivered dose on image quality in coherent scatter computed
62 tomography (CSCT) of the breast. **The present study does not use tomography**
63 **but a system requiring only a simple x,y-scan to perform volumic XRD imaging.**
64 **Its purpose was to determine the dose necessary to detect a 4 mm breast tumor**
65 **using this XRD technique.**

66 We propose an optimized XRD system for use as a second control after
67 conventional mammography with suspicious outcome. Using a convergent col-
68 limation system and a spectroscopic imaging detector, the system combines
69 energy dispersive X-ray diffraction (EDXRD) spectral information at different
70 scattering angles. A multi-angle EDXRD approach **was** suggested by other re-
71 search teams [17, 18] and it was shown that this technique allows an increase
72 of system sensitivity **as well as an increase in** the accessible momentum transfer
73 range [19].

74 The aim of this study was to show that this system **can** detect a small
75 tumor **of about 4 mm** in a fibroglandular tissue background while only requiring
76 exposure to a reasonable (**not more than in conventional mammography**) dose of
77 radiation. This feasibility was demonstrated using simulations of XRD spectra
78 for breast phantoms with different tissue compositions (varying breast density,
79 with or without carcinoma nodule). The ability of the system to distinguish
80 between spectra with or without carcinoma was assessed, and the dose required
81 to obtain faithful distinction between samples was determined. The impact of
82 tumor position and the energy level of the incident spectrum on the required
83 dose were also studied. Finally, one scan slice measurement in the x-direction
84 was simulated and reconstructed to confirm assessed system performances.

85 **2. Theory**

86 *2.1. X-ray diffraction*

Coherent X-ray scattering or Rayleigh X-ray scattering, leading to X-ray diffraction when analyzing crystalline samples, is commonly used to determine the molecular structure of matter. Classically, coherent scattering is explained by the interaction between the electric field associated with the X-ray beam and the distribution of the electron charge in the analyzed sample. Under the action of the incident electric field, electrons oscillate and emit radiation with the same energy as the incident X-ray photon, but in a different direction. Radiation emitted by different electrons in the same or different atoms can constructively interfere to produce a typical X-ray scattering pattern. These patterns depend on the variable χ defined as:

$$\chi = \frac{E}{hc} \cdot \sin\left(\frac{\theta}{2}\right) \quad (1)$$

87 χ is given in nm^{-1} and is proportional to the momentum transferred to the
88 photon causing it to be scattered at an angle θ . E corresponds to the photon en-
89 ergy, h to Planck's constant and c to the speed of light ($1/hc \approx 0.806 \text{ keV}^{-1} \cdot \text{nm}^{-1}$).
90 Hereafter, we will refer to χ as the momentum transfer.

91 The differential cross-section per electron for each solid angle is given by:

$$\frac{d\sigma_{coh}}{d\Omega} = \frac{d\sigma_{Th}}{d\Omega} \cdot f_{IAM}^2(\chi, Z) \cdot s(\chi) \quad (2)$$

92 where $\frac{d\sigma_{Th}}{d\Omega} = r_e^2 \frac{1+\cos^2\theta}{2}$ is the classical Thomson cross-section for a free
93 electron, f_{IAM} is the coherent scatter form factor for independent atoms, ac-
94 counting for interference between X-rays scattered by different electrons from
95 the same atom; s is the molecular interference function accounting for intra-
96 and intermolecular interference. This function corresponds to discrete Bragg
97 peaks for materials with well defined long range orders, such as crystals. In the
98 case of amorphous materials presenting a short-range order, such as biological
99 tissues, s will be a continuous function with an oscillatory behavior around unit
100 value, and a decreasing amplitude as χ tends toward higher values.

101 According to equation (1), XRD spectra can be measured in two ways. Usu-
102 ally, XRD spectra are measured by acquiring the diffraction signal as a function
103 of θ at a fixed beam energy. This technique is called angular dispersive X-ray
104 diffraction (ADXRD). For their acquisition a monochromatic X-ray beam is
105 necessary, which strongly reduces the photon flux if a conventional X-ray tube
106 is used. The second technique, energy dispersive X-ray diffraction (EDXRD),
107 requires X-ray spectroscopic detectors capable of measuring the scattered inten-
108 sity at a fixed scattering angle θ , across a range of energies. As a conventional
109 polychromatic X-ray tube can be used for this method, there is no photon flux
110 problem. In general, EDXRD spectra present a lower resolution than ADXRD
111 as in addition to resolution factors that are common to both methods (e.g. pixel
112 size, object voxel size, angular resolution of the system...) spectral resolution
113 of the detector also degrades the resolution. In ADXRD, the spectral width
114 of the incident spectrum impacts the resolution but this spectral width only
115 exists around the chosen energy whereas in EDXRD each energy bin of the de-
116 tector presents a given spectral width. Nevertheless, EDXRD presents certain
117 advantages compared to ADXRD. First of all, as has already been mentioned,
118 the use of a polychromatic conventional X-ray tube is possible. Furthermore,
119 one detector pixel can acquire the entire XRD pattern of a given object voxel.
120 Therefore, it is possible to acquire the XRD signatures of different object in
121 one pass which significantly increases the acquisition speed. It is also possible
122 to combine the classical ADXRD and EDXRD techniques in order to increase
123 system sensitivity, which will be proposed in the following study.

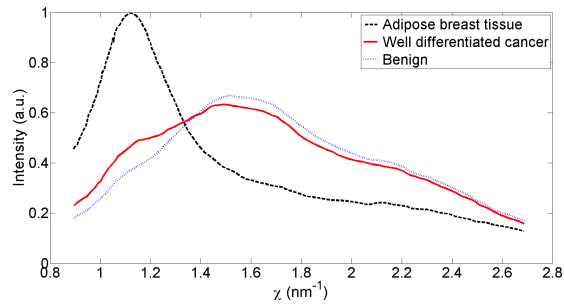
124 2.2. X-ray diffraction in breast imaging

125 The diffraction patterns of biological tissues, which correspond to a molecu-
126 lar structure with short-range order, are characterized by one or more smooth
127 peaks at well-defined momentum transfer values (Fig. 1). Several studies at-
128 tempted to classify different breast tissues using EDXRD [9, 10, 12, 20, 21], or
129 ADXRD [8, 22–25]. A common result of these studies is that healthy adipose tis-
130 sue produces a sharp peak at low momentum transfer values around 1.1 nm^{-1} ,

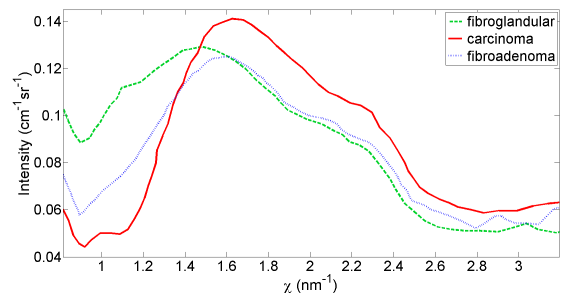
131 while carcinoma presents a broad peak at higher momentum transfer values
132 around 1.6 nm^{-1} (Fig. 1). This higher value corresponds to the maximum of
133 the water scattering signature. Though, the difference between the scattering
134 signatures of cancerous tissue and benign tumor was found to be very small by
135 Pani *et al.* [9] (Fig. 1.a), and it does not seem possible to distinguish these two
136 tissue types by XRD. Kidane *et al.* [10] found fibroadenoma scattering signature
137 to have a maximum around 1.6 nm^{-1} as carcinoma and with scattering inten-
138 sity at lower momentum transfer values between fibroglandular and cancerous
139 tissue (Fig. 1.b). This signature seems to be easier to separate from carcinoma
140 than the pattern determined by Pani *et al.* but more difficult than fibroglan-
141 dular tissue. The attenuation of carcinoma and benign tumors is very similar.
142 However, their shape is different. A fibroadenoma is well defined and sharply
143 demarcated, whereas a carcinoma is ill-defined and has a stellate form. Hence,
144 using the anatomical information from classical mammography or breast CT, it
145 might be possible to distinguish between benign and malignant neoplasm.

146 Therefore, in this study we concentrate on distinguishing between healthy
147 fibroglandular tissue and carcinoma. Both tissue types are very dense and it
148 is often difficult to distinguish between them using conventional mammography
149 because of their very similar absorption coefficients. Their XRD signatures, in
150 contrast, are quite different. Fig. 1.b shows scattering profiles for the two types
151 of tissue, as determined by [10] on a statistically significant number of samples.
152 We used these scattering profiles as reference signatures for this study.

153 The main difference between fibroglandular and cancerous tissues is situated
154 at low momentum transfer values around the fat peak (around 1.1 nm^{-1}), as
155 shown in Fig. 1.b. The χ -values of interest are between 1 nm^{-1} and 2.5 nm^{-1}
156 in the present work.



(a) Breast adipose tissue (black dashed line), cancerous tissue (red line) and benign tumor (blue broken line) [9].



(b) Fibroglandular tissue (light green dashed line), pure carcinoma (red line) and fibroadenoma (blue broken line) [10].

Figure 1: Scattering signatures for different breast tissues.

157 **3. Materials and methods**

158 *3.1. X-ray diffraction system*

159 As explained previously, XRD is proposed to be used as a second control
160 when conventional X-ray mammography results do not give a clear diagnosis.
161 Conventional mammography allows to determine the position of the suspect
162 region in the (x,y) plane, but not its depth within the breast. Hence, the
163 proposed XRD system must be able to target a specific region in the (x,y) plane
164 and to image the whole breast thickness, i.e., to obtain a diffraction pattern as
165 a function of momentum transfer for each depth position in the breast.

166 A classical EDXRD setup consists of a collimated polychromatic X-ray source,
167 a secondary collimation system to select the nominal diffraction angle, and a
168 spectroscopic detector. In our setup, we associate a collimated polychromatic
169 incident pencil beam with convergent secondary collimation targeting (x,y) (Fig.
170 2). This type of system corresponds to a multi-angle EDXRD system, since dif-
171 ferent diffraction angles will be intercepted (convergent system). Furthermore,
172 intercepting different scattering angles makes it possible to use a larger detector
173 surface for the region to be imaged, hence increasing the systems sensitivity.
174 The use of a thin pencil beam means that the diffraction signal is only emitted
175 from a thin line in the sample, which will be referred to as the Z-axis hereafter.

176 Another possible solution to inspect the suspicious region would be CSCT
177 [7, 15, 26]. Batchelar *et al.* [26] used an ADXRD CSCT system working without
178 secondary collimation. This results in an increase of the system sensitivity.
179 Though, the sample to be analyzed must be thin. Otherwise, there would be
180 mixing between different scattering angles and tissues. As we want to analyze
181 the whole breast thickness, this system is not suitable. Ghamraoui *et al.*
182 [15] compared the performance of two CSCT system configurations: fan-beam
183 and pencil-beam configuration. Fan-beam geometry allows to acquire a whole
184 image slice at once but to avoid mixing of different scattering angles strong
185 collimation is required, which significantly reduces system sensitivity. Pencil
186 beam configuration requires less collimation. Though, measurement lines (or

187 translations) and sample rotation are required, which is not always easy in
 188 clinical routine. They also investigated the use of multiplexed-beams geometry
 189 which is faster than pencil beam configuration but still requires sample rotation
 190 typical for CT imaging.

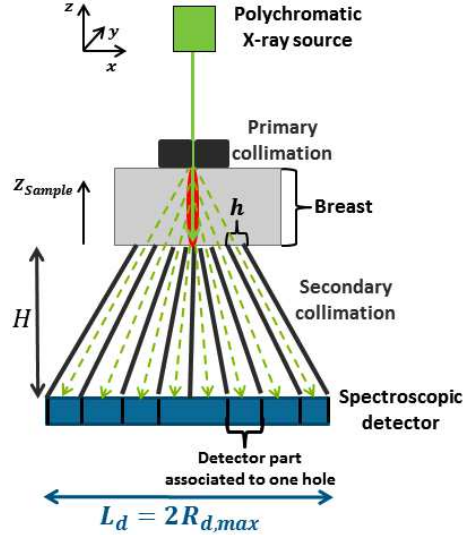
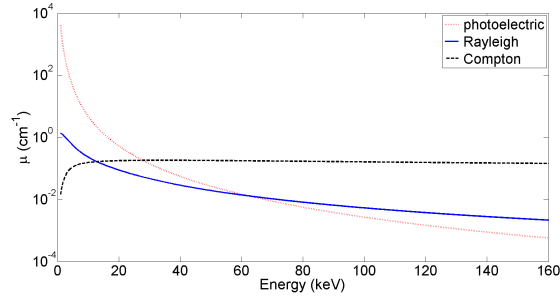


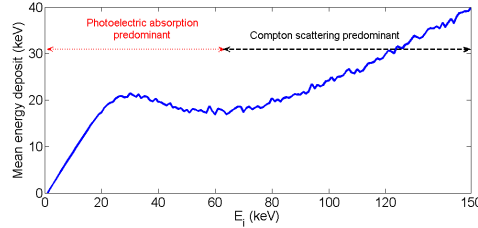
Figure 2: Schematic representation of a system combining EDXRD information at multiple scattering angles: a polychromatic incident pencil beam, a convergent (multifocal) secondary collimation system and a spectroscopic detector.

191 3.1.1. Incident X-ray beam

192 The incident X-ray source was simulated using SpekCalc [27]. The anode
 193 material was chosen to be tungsten. The choice of a tungsten anode instead
 194 of a molybdenum as normally used in mammography, can be justified by the
 195 fact that molybdenum presents low bremsstrahlung intensity compared to its
 196 characteristic peaks. In EDXRD, it is important to have a more continuous
 197 distribution of photons over the different energies of the incident spectrum in
 198 order to cover the required χ -range at the chosen scattering angle. Hence, tung-
 199 sten is a suitable choice. A 0.2 mm copper filter was used to suppress photons
 200 below 20 keV as these photons would be almost entirely absorbed by photo-
 201 electric interaction (Fig. 3) producing a dose deposit without generating any



(a) Linear attenuation coefficients.



(b) Mean energy deposit.

Figure 3: a) Linear attenuation coefficients of water for different types of interaction. b) Mean energy deposit (multiple interactions included) for one photon in 50 mm of a material with average chemical composition of breast tissue as a function of incident photon energy (generated with PENELOPE 2008 [28]).

202 diffraction signal. Similarly, energies above 100 keV appear superfluous as the
 203 probability of Rayleigh scattering becomes very low compared to Compton scat-
 204 tering. This is illustrated by Fig. 3 showing the linear attenuation coefficients
 205 of water (a) and the mean energy deposit (generated with PENELOPE 2008
 206 [28]) in 50 mm of a material whose chemical composition is close to average
 207 breast tissue (H: 9.82%, C: 33.15%, N: 3.41%, O: 51.96%, P: 0.50%, S: 0.52%,
 208 K: 0.63% [29], percentages correspond to mass fractions). Hence, the reference
 209 incident X-ray spectrum in this work is between 20 and 100 keV. Though, to
 210 study the impact of the maximum energy of the incident X-ray spectrum on
 211 system performances, a range of tube voltages, between 40 kV and 150 kV, was
 212 tested.

213 *3.1.2. Secondary collimation*

214 Two possible convergent collimation systems were considered here: a mono-
215 focal system and a multifocal system. Monofocal collimation systems only target
216 at one point in the object and require a depth scan, whereas multifocal systems
217 focus on several sample points simultaneously, and can acquire the whole depth
218 in one shot. Both systems require an (x,y)-scan to image the region identified as
219 suspect by mammography. A convergent monofocal system has been considered
220 by Malden and Speller [17] who used a multi-angle approach for baggage inspec-
221 tion. Though, as it is focused on only one voxel this kind of system would also
222 require a scan in the z-direction. This would significantly increase dose delivery
223 and it appears too complex for routine use in practice. Hence, this article only
224 presents results obtained with a multifocal collimation system able to image the
225 whole sample thickness in one go. A schematic representation of a multifocal
226 collimation system is illustrated in Fig. 2.

227 To obtain the best possible resolution and sensitivity in all directions, a con-
228 ical secondary collimation setup was chosen, in line with the intrinsic symmetry
229 of XRD. Circular symmetry for the secondary collimation was previously sug-
230 gested by Harding and Schreiber [30] for instance. However, their system is a
231 mono-angle EDXRD system with one slit focused on only one object voxel,
232 whereas the collimation system proposed here corresponds to a multi-angle
233 EDXRD system with several slits focused on a whole sample line. It is composed
234 of seven hollow cones nested one inside the other. A beam-stop was placed in the
235 center to stop transmission signal. The collimation system in Fig. 2 represents
236 a cross-section of this type of collimation system.

237 The collimation system was designed without multiplexing, **which means**
238 **that each detector pixel only receives the diffraction signal from a single object**
239 **voxel. In the case of the presented system, this means that each detector pixel**
240 **only receives the diffraction signal from a single collimation hole (a concentric**
241 **annulus in our case) as the system was conceived to adress only one connected**
242 **depth-region in the target.** Therefore, the detector was divided into as many

243 parts as the number of holes, and each part was associated with a single hole
 244 (Fig. 2). It has to be noted that a detector part contains several pixels. The total
 245 detection surface is the same for each part. Fig. 4 illustrates the subdivision of
 246 the detector and the definition of a pixel annulus.

247 Each hole targets a different sample depth position (multifocal collimation)
 248 and covers a well defined region in the sample. Collimation height H and hole
 249 aperture h were adjusted in order to intercept the required momentum transfer
 250 range (combination of incident photon energies and covered scattering angles)
 251 between $\chi = 1$ and 2.5 nm^{-1} (Fig. 1) and to obtain a momentum transfer
 252 resolution of at least 0.2 nm^{-1} while maintaining system sensitivity as high
 253 as possible. Table 1 summarizes the system parameters used for this study.
 254 Resolution was mostly influenced by collimation height and hole size. "Pixel
 255 size" (annular thickness) was not limiting if it remained small (around 1 mm
 256 or smaller). The number of holes was fixed in order to have as much holes by
 257 respecting a septa thickness of at least 0.3 mm and by targeting the desired
 258 scattering angles. Covered scattering angles range from 0.1° to 11° , where each
 259 hole intercept a different range of angles. The first hole corresponds to low
 260 scattering angles (up to 5°), whereas the last hole covers the highest scattering
 261 angles. Collimator material was simulated as iron, which is less expensive than
 262 tungsten and easier to manufacture. Septa thickness was about 1 mm at detector
 263 side and between 0.3 and 0.5 mm at sample side.

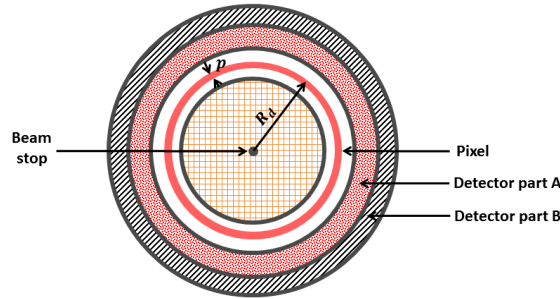


Figure 4: Schematic representation of detector partitioning (detection surface of detector part A = detection surface of detector part B). One detector part contains more than one pixel. The red pixel, which is represented here, is part of the white detector part.

Table 1: System parameters. H : collimation height; h : collimation hole size; p : annular thickness; L_d : detector dimension.

Number of holes	H (mm)	h (mm)	p (mm)	L_d (mm)
7	230	0.8	1.0	100

264 Obviously, eventhough this kind of collimation allows to collect the scattering
 265 signal following the whole annulus associated to one scattering angle, it strongly
 266 restricts the number of detected photons compared to the number of incident
 267 photons. Coded aperture systems combining EDXRD and ADXRD [31, 32]
 268 use less collimation and can also be used to obtain a 2D image. However, this
 269 kind of systems seems more adequate for discrete scattering signatures than
 270 for continuous tissue signatures. Eventhough the number of detected photons
 271 is higher, the amount of information that can be retrieved is not necessarily
 272 higher because of ambiguity between scattering angle and momentum transfer
 273 (due to multiplexing) with coded apertures, **which seems to be more difficult**
 274 **to resolve for amorphous spectra than for crystalline spectra.** The amount of
 275 information carried by the photons is not the same for each detected photon.
 276 We tested to add slight multiplexing to our system in order to increase system
 277 sensitivity, but the required dose to detect **the** small tumor also increased.

278 3.1.3. Detector

279 For this study, we considered a 5 mm thick 2D 10×10 mm² spectroscopic
 280 CdZnTe detector with 2.5 mm anode pitch. CdZnTe is a room temperature
 281 semiconductor detector with high resistivity ($\rho = 5 \cdot 10^{10} \Omega \cdot cm$), good transport
 282 properties ($\mu\tau = 5 \cdot 10^{-3} cm \cdot V^{-1}$) and a crystallinity compatible with fabrication
 283 of devices measuring several cm^3 . The thickness of 5 mm is hence feasible and
 284 is well appropriate for the considered range of energies. In a previous study [33],
 285 we showed that a spatial resolution of 0.4 mm can be achieved at 60 keV with
 286 this detector geometry using transient signal processing, a technique known as

287 subpixel positioning. The advantage of this technique is that it can improve
 288 spatial resolution without degrading the spectral response by charge sharing
 289 (due to smaller anode size). Here, 1 mm subpixel size was used for our system
 290 simulations. The associated ASIC (Application-Specific Integrated Circuit) was
 291 based on IDeFX-HD [34], which combines low noise and low power. In practice,
 292 the average energy resolution was about 2.5% at 122 keV.

293 Using these characteristics, a detector response matrix (DRM), accounting
 294 for limited energy resolution of the detector, was obtained using Tasmania, a
 295 simulation environment developed in our laboratory. It gives the probability
 296 of detecting a given amplitude A knowing the incident photon energy E_d on
 297 the detector. This detector response model takes into account the following
 298 elements: radiation (photons & photoelectrons) transport based on PENELOPE
 299 [28], a 3D electric field model (for applied and weighting fields), 3D charge
 300 carrier transport (diffusion, drift, trapping & Coulomb repulsion) [35], a detailed
 301 noise model (detector & readout electronics) and a behavioral model of analog
 302 electronics (shaping, trigger & peak detector).

303 3.1.4. Sensitivity and resolution

304 System sensitivity only depends on the geometric parameters of the acquisi-
 305 tion system and not on the interaction cross-section of the sample. The sensitiv-
 306 ity achieved with detector position r for the position in the sample Z_{Sample} can
 307 be defined as the ratio of the surface (Fig. 5.a), at detector level, of an isotrop-
 308 ically radiating point located at Z_{Sample} to the intercepted detector surface at
 309 detector position r :

$$dS(Z, r) = \int_0^{2\pi} \frac{Zrdr}{4\pi(r^2 + Z^2)^{\frac{3}{2}}} d\varphi \quad (3)$$

310 where $Z = Z_{Sample} + H + g$ with g the gap between secondary collimation and
 311 sample. Integration over the cylindrical coordinate, φ , is necessary to consider
 312 the whole detector annulus of radius r and thickness dr (Fig. 5.b). To obtain a
 313 system sensitivity in the pixel range with a radius, R_d , from the center to the

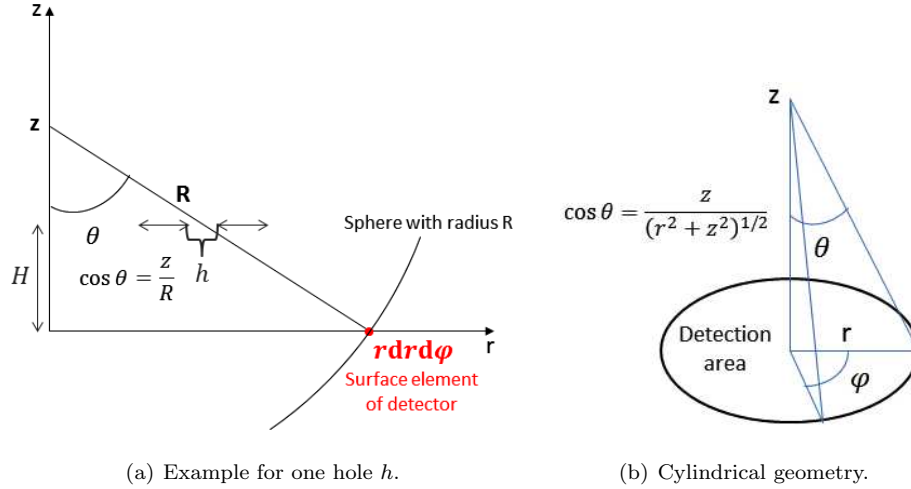


Figure 5: Schematic illustration of sensitivity calculations.

314 sampling point, Z_{Sample} , it is sufficient to integrate all r from which Z_{Sample}
 315 can be "seen" and which are part of the pixel.

316 Fig. 6.a shows the sensitivity distribution on the detector (detector position
 317 R_d) and in the sample (depth position in the sample Z_{Sample}) which was cal-
 318 culated analytically. The higher the sensitivity value the more of the photons
 319 (isotropically) emitted from Z_{Sample} can be detected at a given detector posi-
 320 tion R_d . A gap of 10 mm between the secondary collimation and the breast
 321 sample was considered to produce maximum sensitivity at the center of the
 322 breast. The size of the gap was determined by considering the analytically cal-
 323 culated sensitivity profile in the sample for the case, where the sample and the
 324 secondary collimation are in contact. In this case, maximum sensitivity was at
 325 $Z_{Sample} = 35$ mm ($Z_{Sample} = 0$ mm corresponds to the sample edge at sec-
 326 ondary collimation side). The different detector parts were obviously sensitive
 327 to different sample zones. Hence, the system is a multifocal collimation system.
 328 This multifocal nature was also confirmed by the sensitivity profile in the sam-
 329 ple represented in Fig. 6.b, which corresponds to the sum over R_d of Fig. 6.a.
 330 The systems sensitivity was good almost throughout the samples thickness with
 331 its maximum, which is indeed at the center ($Z_{Sample} = 25$ mm). Because it is

332 close to the pencil beam axis (Z-axis) where the diffraction signal originates, the
 333 first hole is sensitive to the whole sample thickness (Fig. 6.a), meaning that its
 334 spatial resolution is very poor. Global resolution of the system is significantly
 335 deteriorated by the first hole, but it allows detection of features in the lower
 336 sample regions and thus increases the systems overall sensitivity as a whole.

337 The overall system performance of the collimation was assessed based on
 338 detective quantum efficiency (DQE) and modulation transfer frequency (MTF)
 339 calculations [19, 36]. It has to be noted this is not the commonly used definition
 340 of DQE for detectors. Here it indicates the performance of the collimation
 341 system associated to a given detector area. This wider concept of DQE was also
 342 considered by Starck *et al.* [37] to characterize gamma camera systems. We
 343 adapted these calculations do XRD imaging systems [19]. In photon counting
 344 systems (Poisson noise) such as XRD systems, the DQE is the product of the
 345 sensitivity and squared modulus of the MTF [36]: $DQE(\nu) = S \cdot MTF^2(\nu)$.

346 We are able to determine the MTF of one pair hole-pixel ($MTF_{hp}(\nu_z)$). Use
 347 of the DQE allows to obtain a synthetical figure of merit combining sensitiv-
 348 ity and resolution [19]. The DQE of a pair hole-pixel is given by the squared
 349 $MTF_{hp}(\nu_z)$ weighted by its sensitivity S_{hp} . To get the DQE of the whole colli-
 350 mation system, the contributions of the different pairs hole-pixel can simply be
 351 summed if there is no multiplexing [36]:

$$DQE(\nu_z) = \sum_{pixels} S_{hp} \cdot MTF_{hp}^2(\nu_z) \quad (4)$$

352 The global spatial resolution, \mathcal{R} , can be determined from the modulation
 353 transfer function curve:

$$\frac{1}{\mathcal{R}} = 2 \int_0^{+\infty} \frac{DQE(\nu_z)}{DQE(0)} d\nu_z = 2 \int_0^{+\infty} MTF^2(\nu_z) d\nu_z \quad (5)$$

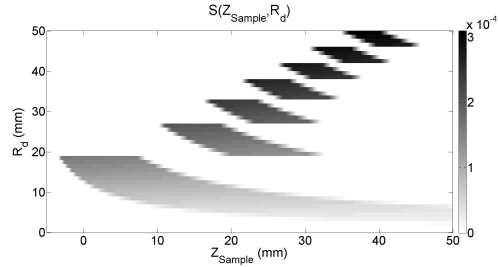
354 This definition is consistent with the full width at half maximum (FWHM)
 355 for a rectangular gate-shaped point spread function. Angular $MTF_{hp}(\nu_\theta)$ is de-
 356 termined by geometrical considerations linking z and θ , and momentum transfer
 357 $MTF_{hp}(\nu_\chi)$ can be calculated using the relationship between θ and χ (Eq. 1).

358 The calculated overall system resolutions are summarized in table 2. With
 359 9.6 mm in the direction of the samples thickness, the spatial resolution is low,
 360 but it is nevertheless better than other XRD systems, which do not offer any
 361 depth resolution. Some XRD imaging techniques such as CSCT [7, 16] and
 362 coded aperture coherent spectral imaging [31, 38] allow to obtain better spatial
 363 resolution in beam direction. Greenberg *et al.* [38], for instance, obtained a
 364 spatial resolution of 5 mm in beam direction. However, contrast is lost due
 365 to multiplexing inherent in coded aperture methods. In CSCT the resolution
 366 is good but in clinical routine it is not always easy to rotate while imaging,
 367 especially in breast imaging. We seek to propose an imaging system able to
 368 acquire the whole sample thickness in one go with a satisfying spatial resolution
 369 and having a good sensitivity while maintaining the best possible momentum
 370 transfer resolution without the need of rotating movements.

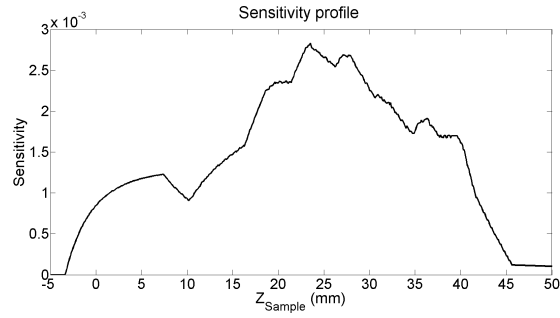
371 The momentum transfer resolution meets the constraint of 0.2 nm^{-1} for
 372 almost every energy tested due to adequate angular resolution. Integration
 373 over the whole incident X-ray spectrum (between 20 and 100 keV) leads to
 374 an average momentum transfer resolution of about 0.07 nm^{-1} . However, the
 375 calculations did not take the detectors energy resolution into account because
 376 we were interested in proposing the best possible collimation system. Doing
 377 so slightly deteriorates the momentum transfer resolution, as this resolution
 378 depends on both angular and spectral resolution:

$$\Delta\chi = \frac{E}{2hc} \cdot \cos\left(\frac{\theta}{2}\right) \Delta\theta + \frac{1}{hc} \sin\left(\frac{\theta}{2}\right) \Delta E \quad (6)$$

379 If a mean energy resolution of 3 keV is considered, this corresponds to 5%
 380 at 60 keV. This leads to a resolution of 0.1 nm^{-1} at 2 nm^{-1} . At 20 keV this
 381 resolution will be lower and 100 keV it will be higher, but in average the global
 382 momentum transfer resolution is not worse than the required 0.2 nm^{-1} . In
 383 the following simulation study both contributions (angular resolution of the
 384 collimation and energy resolution of the detector) are taken into account.



(a) Sensitivity distribution.



(b) Sensitivity profile.

Figure 6: Sensitivity distribution and sensitivity profile of the simulated X-ray diffraction system across the sample (sample starts at 0 and ends at 50 mm).

Table 2: Resolutions of the X-ray diffraction system considered (the spectral resolution of the detector not taken into account).

Spatial (mm)	Angular ($^{\circ}$)	χ at 20 keV (nm^{-1})	χ at 60 keV (nm^{-1})	χ at 100 keV (nm^{-1})	χ at 150 keV (nm^{-1})
9.6	0.21	0.029	0.09	0.15	0.22

385 *3.2. Simulations*

386 Our X-ray diffraction system’s capacity to distinguish between carcinoma
387 and fibroglandular tissue was assessed using Monte-Carlo simulations of the
388 whole system and a breast phantom. These simulations were performed with
389 PENELOPE [28], by adapting cross-sections for coherent scattering to take
390 intra- and intermolecular radiation interference, i.e., X-ray diffraction, into ac-
391 count. Cross-sections used in PENELOPE for Rayleigh scattering only contain
392 the Thomson cross-section and the coherent scatter form factor (Eq. 2). We
393 replaced these cross-sections by the diffraction signatures determined by [10]
394 (Fig. 1.b).

395 Simulations take into account all kinds of interaction (Rayleigh scattering,
396 Compton scattering, Photoelectric absorption, multiple scattering, fluorescence)
397 and all possible locations of interaction (collimation, phantom, detector).

398 *3.2.1. Breast phantom*

399 The simulated breast phantom was a 50 mm thick, and 150 mm diameter
400 cylinder of adipose tissue containing an ellipsoid of fibroglandular tissue (**axis**
401 **in x- and y-direction: 70 mm**) corresponding to a region with altered compo-
402 sition. To assess the impact of the thickness (**i.e. the axis in z-direction**) of
403 fibroglandular tissue, this ellipsoid was simulated in a range of thicknesses: 20,
404 30 and 40 mm. This allowed us to verify whether high density breast tissue
405 can be imaged with XRD. A small spherical carcinoma nodule was located in
406 the center of the phantom, in the case of a phantom with tumor. The diameter
407 of this nodule was about 4 mm, which corresponds to a very small tumor size.
408 In scintimammography, for instance, tumors smaller than 6 mm are difficult to
409 detect [39, 40]. Fig. 7 shows a schematic representation of the breast phantom.

410 As system sensitivity is not the same over the whole of the samples thickness,
411 it is important to study the impact of tumor position on its detectability. The
412 tumor was always located in the fibroglandular mass at this location will result
413 in doubtful mammography results. Therefore, tumor position variation study
414 was realized with 40 mm fibroglandular thickness. Four tumor offset positions

415 were tested: +20 mm, +10 mm, -10 mm and -20 mm. A positive tumor offset
 416 corresponds to a greater distance between tumor and detector, while a negative
 417 offset corresponds to a shorter distance.

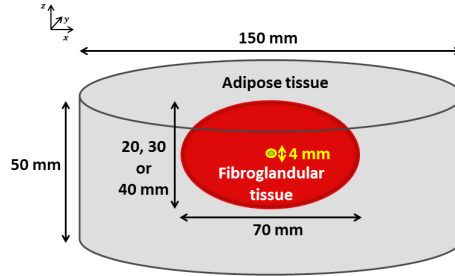


Figure 7: Simulated breast phantom presenting a nodule (yellow sphere) composed of pure carcinoma.

418 Scans in x-direction (N.B.: scans in y-direction were not simulated as they
 419 are equivalent to scans in x-direction.) were simulated with and without tumor
 420 for a fibroglandular thickness of 30 mm and incident spectra at 60 kVp and
 421 100 kVp. The scan step was chosen to be 1 mm.

422 3.3. Data analysis

423 3.3.1. Separation power and required incident photon number

424 The contrast to noise ratio (CNR) is a measure of the separation power of a
 425 given imaging system and is defined as:

$$CNR = \frac{\Delta M}{\sigma} \quad (7)$$

426 where $\Delta M = M_A - M_B$ corresponds to the difference between the expected
 427 signal intensities M_A and M_B produced by materials A and B, and σ corre-
 428 sponds to the standard deviation of the noise.

429 Diffraction measurements follow a Poisson law, but for CNR calculations a Gaus-
 430 sian approximation ($\mu = \sigma^2 = \lambda$, where λ is the Poisson parameter) of photon
 431 noise was used.

432 If A and B are the two tissue types to be distinguished (carcinoma and fibrog-

433 glandular tissue), using the Gaussian approximation, the squared CNR is given
 434 by:

$$CNR^2 = \sum_i \frac{(M_{A,i} - M_{B,i})^2}{\sigma_i^2} \quad (8)$$

435 where M_A and M_B are the expected diffraction signatures of A and B nor-
 436 malized by the number of incident photons, and $\sigma_i^2 = M_{A,i} + M_{B,i}$ the standard
 437 deviation of $M_A - M_B$ on channel i .

438 In fact, the CNR^2 defined above corresponds to the quadratic distance be-
 439 tween the two distributions, A and B, per incident photon. Hence, the inverse
 440 of the CNR^2 corresponds to the number of photons, $N_{ph,1\sigma}$, requested to obtain
 441 a distance of one standard deviation between the two distributions. This is a
 442 very low-level separation. Hereafter, a separation of 3σ will be considered:

$$N_{ph,3\sigma} = \frac{9}{CNR^2} \quad (9)$$

443 3.3.2. Dose estimation

444 The radiation dose was estimated using the incident X-ray spectrum, S_{inc} ,
 445 the mean energy deposit for one photon in 50 mm of breast tissue similar ma-
 446 terial, E_{mean} , as a function of incident photon energy, E_i (Fig. 3.b), and the
 447 calculated incident photon number, N_{ph} , required to obtain the desired separa-
 448 tion between XRD spectra with and without carcinoma.

449 The mean total energy deposit per photon, D_E , for a given incident spectrum
 450 is calculated using:

$$D_E = \frac{\sum_{E_i} E_{mean}(E_i) \cdot S_{inc}(E_i)}{\sum_{E_i} S_{inc}(E_i)} \quad (10)$$

451 The result is expressed in keV. For an incident spectrum with a maximum
 452 energy of 100 keV, the mean total energy deposit will be about 18.88 keV.
 453 Knowing the required number of incident photons, the required mean dose is
 454 given by:

$$D = \frac{D_E \cdot 1.6 \cdot 10^{-16} \cdot N_{ph}}{m_{irr}} \quad (11)$$

455 where $1.6 \cdot 10^{-16}$ is the conversion factor to transform keV into joules (J),
 456 and m_{irr} corresponds to the directly irradiated mass. In the present case, the
 457 irradiated mass is about $5 \cdot 10^{-8}$ kg (i.e. pencil beam surface \times sample thickness
 458 \times sample density = $10^{-6} m^2 \times 50 \cdot 10^{-3} m \times 1 kg \cdot m^{-3}$).

459 Note that this dose corresponds indeed to the total dose deposited in the
 460 whole breast thickness. The mean energy deposit for one photon E_{mean} was
 461 obtained by Monte-Carlo simulations taking into account every possible inter-
 462 action within the whole sample thickness.

463 3.3.3. Reconstruction method

464 The simulated scan measure m is modeled linearly by:

$$m(A, R_d, x) = \sum_{Z,i} Resp(A, R_d, Z, i) \cdot t(Z, i, x) \quad (12)$$

465 where x corresponds to the scan position and $Resp(A, R_d, Z, i)$ to the sys-
 466 tem response matrix depending on the detected amplitude A , the position on
 467 the detector R_d , Z and the tissue type i (adipose tissue, fibroglandular tissue,
 468 carcinoma). $t(Z, i, x)$ is a coefficient indicating whether tissue i is present at
 469 the position Z and detected at scan position x . As there is no tissue mixing
 470 in the breast phantoms considered here, it is either equal to zero (tissue i not
 471 present) or to one (tissue i present).

472 The aim of reconstruction is to process measurements, $m(A, R_d, x)$, to es-
 473 timate the material coefficients, $t(Z, i, x)$, which can be represented in a color
 474 image, using material i as a single color channel.

475 Methods using material decomposition were also suggested by other authors,
 476 Westmore *et al.* [7] who proposed a non-negative least squares fitting algorithm
 477 to estimate the amount of a given material, or Ghammraoui *et al.* [16] who
 478 suggested a version of maximum likelihood expectation maximization algorithm
 479 with ordered subsets.

480 In this study, we used the maximum likelihood expectation maximization
 481 algorithm for reconstruction[41]. This algorithm is based on the iterative max-
 482 imization of the log-likelihood function, which is very common in the likelihood
 483 maximization framework.

484 The estimated measurement, \tilde{m} , can be written assuming an ideal direct
 485 system operator, \mathcal{F} :

$$\tilde{m}(A, R_d, x) = \sum_{Z,i} \mathcal{F}(A, R_d, Z, i) \cdot t(Z, i, x) \quad (13)$$

486 The most significant noise source in diffraction is photon noise, which by its
 487 nature follows a Poisson law with parameter $\sum_{Z,i} \mathcal{F}(A, R_d, Z, i) \cdot t(Z, i, x)$. A
 488 maximum likelihood approach consists in determining:

$$\hat{t} = \arg \max_{t \geq 0} P(m | t) \quad (14)$$

An iterative solution is thus given by the following algorithm [41]:

$$\hat{t}^{n+1}(Z, i, x) = \frac{\hat{t}^n(Z, i, x)}{\sum_{A, R_d} \mathcal{F}(A, R_d, Z, i)} \sum_{A, R_d} \frac{\mathcal{F}(A, R_d, Z, i) \cdot m(A, R_d, x)}{\sum_{Z, i} \mathcal{F}(A, R_d, Z, i) \cdot \hat{t}^n(Z, i, x)} \quad (15)$$

489 where \hat{t}^{n+1} is the estimate of t at the n th iteration. Choosing a positive
 490 value for \hat{t}^0 will ensure that the final results are non-negative. Here, a uniform
 491 initialization was used.

492 4. Results and discussion

493 Fig. 8 shows two sample XRD spectra (normalized by the number of incident
 494 photons) to be distinguished; the fibroglandular region was 30 mm thick and
 495 the incident spectrum had a maximum energy of 100 keV. These spectra were
 496 simulated for $x = 0$ and $y = 0$ corresponding to the phantom center in x,y-
 497 plane. All the following results are given for this position except the scan slice
 498 reconstruction, where x-position varied. The gap between secondary collimation
 499 and object was 10 mm for each simulation in this work.

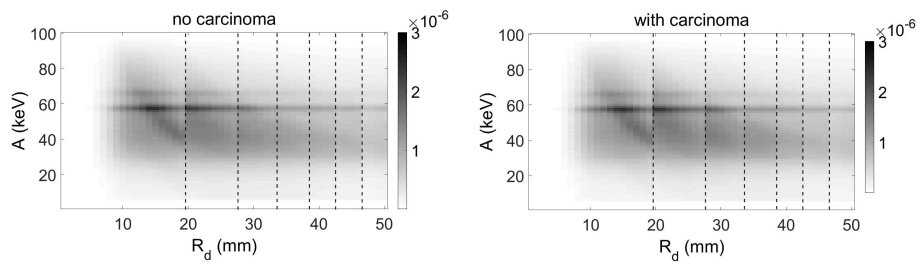
500 The segments visible in the spectra and even more clearly in their difference
501 correspond to the limits of the different collimation holes. The dotted lines in
502 Fig. 8.c indicate these limits. By summing the normalized spectra from Fig. 8
503 in both directions, the object depending global sensitivity can be determined,
504 which takes into account geometrical factors as well as the sample interaction
505 cross-section. It corresponds to the ratio between the number of incident pho-
506 tons on the sample and the number of detected photons. This is not exactly the
507 same quantity as defined in section 3.1.4, which is purely geometrical (which
508 proportion of photons emitted isotropically at a given Z can be detected by the
509 system) and does not take into account interaction cross-section in the sample.

510 In this case, object depending global sensitivity is approximately $2 \cdot 10^{-3}$.
511 Multiplication of this value by the number of incident photons gives the total
512 number of photons detected. The CNR^2 per incident photon is about $2 \cdot 10^{-6}$,
513 which is very low, explaining why the differences between the two XRD spectra
514 (without tumor (Fig. 8.a); with tumor (Fig. 8.b)) are hardly visible. Fig. 8.c
515 shows the difference spectrum in absolute value. The difference to be detected
516 is only in the order of a few percent (difference values per pixel and per channel
517 between 10^{-8} and 10^{-7} compared to XRD spectrum values per pixel and per
518 channel of about 10^{-6}).

519 Hereafter, the photon number and associated dose are given for a separation
520 of 3σ between XRD spectra with and without tumor. This degree of separation
521 corresponds to an almost perfect separation based on the associated analyti-
522 cally calculated ROC curve [42]. The number of incident photons required is
523 determined using equation 9 and will be around $5 \cdot 10^6$. The associated dose is
524 calculated using equation 11. Thus, all given dose values correspond to the dose
525 delivered to the irradiated sample volume over the whole sample thickness.

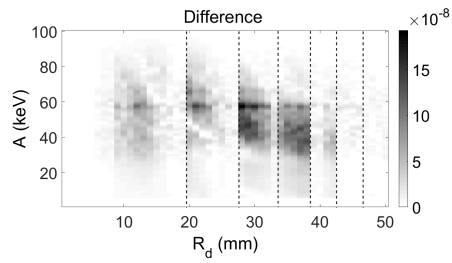
526 4.1. Fibroglandular thickness

527 The results for the required photon number and the corresponding dose
528 for an incident spectrum with a maximum energy of 100 keV and different
529 fibroglandular thicknesses are summarized in table 3. Fibroglandular thickness



(a) XRD spectrum without tumor.

(b) XRD spectrum with tumor.



(c) Difference spectrum (absolute value).

Figure 8: Simulated XRD spectra ($x = 0$, $y = 0$, 10 mm gap between sample and secondary collimation) normalized for the number of incident photons and the absolute value of their difference. Fibroglandular thickness: 30 mm; incident spectrum maximum energy: 100 keV. The difference to be detected is minute compared to XRD spectrum values. Dotted lines correspond to the limits of the detector parts addressed by the different holes.

530 has a negligible impact on the number of photons required, thus averaging at
 531 about $4 \cdot 10^6$ for a corresponding dose of about 0.24 mGy. This dose is low
 532 compared to conventional mammography, where the dose delivered is between
 533 1 and 3 mGy [43–45].

534 Hence, scattering signatures for cancerous tissues and fibroglandular tissues
 535 are sufficiently decorrelated to be distinguished even when the number of de-
 536 tected photons is small. Furthermore, as the required dose does not significantly
 537 vary with fibroglandular tissue thickness, high density breast regions pose no
 538 problems in XRD, unlike in conventional mammography. In fact, as used tube
 539 voltage is significantly higher than in classical mammography photons have
 540 higher energy and reduction of expected counts due to increased breast den-
 541 sity is less significant. Moreover, the incident spectrum was filtered in order to
 542 remove photons at energies below 20 keV in order to avoid unnecessary dose de-
 543 posit by photons that are almost completely absorbed, whereas mammography
 544 typically uses photons at these energies.

Table 3: Incident photon number and dose required to obtain a separation of 3σ for an incident spectrum with maximum energy of 100 keV.

Fibroglandular thickness (mm)	Required photon number	Required dose (mGy)
20	$3.85 \cdot 10^6$	0.232
30	$4.20 \cdot 10^6$	0.253
40	$4.12 \cdot 10^6$	0.244

545 4.2. Influence of different maximum energies

546 Fig. 9 shows the dose received by samples analyzed using our optimized sys-
 547 tem, as a function of the maximum energy of the incident spectrum for a phan-
 548 tom with 40 mm thick fibroglandular tissue section with a tumor at the center of
 549 the field of view. A minimum was observed at 60 and 70 keV corresponding to a

550 dose of about 0.21 mGy. For incident spectra with lower maximum energy, the
 551 combination of photon energy and intercepted angles is less appropriate and
 552 absorption remains higher than coherent scattering. At higher energies, the
 553 probability of absorption and coherent scattering continue to decrease, whereas
 554 Compton scattering probability remains constant. Hence, the proportion of sig-
 555 nal due to Compton scattering increases steadily with increasing photon energy,
 556 causing blurring of the measured XRD spectrum and unnecessary radiation ex-
 557 posure. However, even though the received dose increases with higher maximum
 558 energy of the incident spectrum, the total dose still remains low and acceptable
 559 compared to conventional mammography.

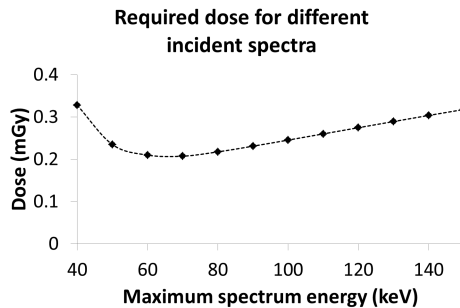


Figure 9: Dose required to separate (3σ separation) phantoms (40 mm fibroglandular thickness) with and without tumor as a function of the maximum energy of the incident X-ray spectrum.

560 *4.3. Impact of tumor position*

561 The dose required to distinguish between spectra with and without tumor for
 562 different tumor offsets and maximum incident spectrum energies are presented
 563 in Fig. 10. If the tumor is located in the center (no offset), the required dose is
 564 the lowest. In fact, the maximum of sensitivity is in the center and the tumor
 565 can be "seen" by five holes (Fig. 6.a). If a tumor offset is introduced, the
 566 difference between spectra with and without tumor will not be detected by the
 567 same holes, as the system has a variable sensitivity distribution. The first hole
 568 always detects part of the difference, as it is sensitive throughout the sample

569 thickness. Required doses are slightly higher for other tumor positions but as
 570 long as the tumor is in the field of view (sensitivity zone), these doses stay very
 571 small. The detection of the tumor for the +20 mm offset, where the tumor
 572 was positioned at $Z_{Sample} = 45$ mm, requires an approximately 5-fold higher
 573 dose. This position corresponds to a very low sensitivity region for the presented
 574 system configuration. However, the total dose received still remains not higher
 575 than with conventional mammography (1-3 mGy).

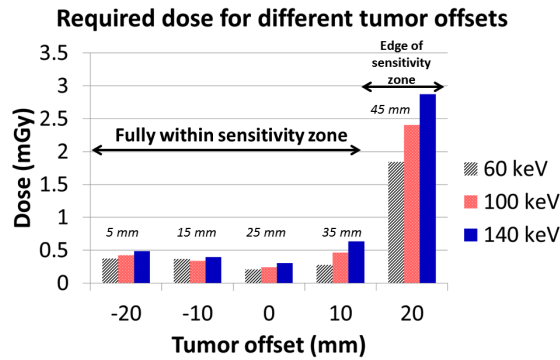


Figure 10: Dose required to distinguish (3σ separation) between spectra with and without carcinoma depending on the position of the tumor within the sample (depth).

576 4.4. Reconstruction results

577 Fig. 11 shows an example of a simulated XRD spectrum for a phantom
 578 (30 mm fibroglandular tissue thickness, 100 kVp incident spectrum) with a
 579 tumor at its center, for scan position $x=0$, corresponding to the center of the
 580 phantom in the x,y -plane. The number of incident photons was about $5 \cdot 10^6$,
 581 corresponding to approximately 10^4 detected photons and to a dose deposit of
 582 about 0.3 mGy. This dose is consistent with the required dose determined in the
 583 previous parts of the study and with the dose given by Ghammraoui *et al.* [15].
 584 With an incident dose of about 0.5 mGy a small tumor of similar size could be
 585 reconstructed in a CSCT image when pencil beam geometry was used.

586 The number of photons per channel is very low, producing a relatively noisy
 587 spectrum. However, the number of incident photons is within the order of

588 magnitude determined previously to obtain a 3σ separation between phantoms
589 with and without tumor.

590 Each scan slice was simulated using the same incident photon parameters,
591 and the image of the breast phantom was reconstructed (Fig. 12) using the
592 previously presented reconstruction method. It should be noted that the field
593 of view for the image was set smaller than the phantom height. Hence, only
594 5 mm of adipose tissue is visible on the upper and lower parts of the image,
595 rather than 10 mm.

596 This reconstruction clearly shows that the tumor will only be reconstructed
597 if it is actually in the simulated phantom slice (Fig. 12.b and fig 12.d), and
598 therefore no false positive results **should be produced for a tumor positioned**
599 **in the center of the phantom**. The tumor is sharper and more intense in the
600 reconstruction at 60 kVp. This is consistent with the fact that the optimal
601 incident spectrum to detect the small tumor was found to be at 60 kVp. Hence,
602 using this incident spectrum the best tumor reconstruction should be obtained.
603 Though, compared to reconstructions at 60 kVp, reconstructions at 100 kVp
604 present fewer edge artifacts at the limit between fibroglandular tissue and adi-
605 pose tissue, especially at low depths within the sample. This difference is due
606 to lack of information in the momentum transfer space at low depths. In fact,
607 as can be seen in Fig. 6.a, the first hole in the collimation system is the only
608 hole sensitive to low depth values. Though the corresponding scattering angles
609 are also low because the corresponding detector part is close to the center in
610 the x,y-plane (small R_d , Fig. 2 and Fig. 4). Thus, to cover the same momentum
611 transfer range as for other holes intercepting higher scattering angles (higher R_d
612 values), higher energies are needed. It appears that the information obtained at
613 60 keV maximum energy is not sufficient to distinguish between fibroglandular
614 and adipose tissue. Reconstruction artifacts (i.e. detection of carcinoma) in the
615 upper corners of the images at 60 kVp are also caused by the lack of informa-
616 tion in momentum transfer space at this energy level. As for low depths, these
617 high depth values are only covered by the first hole with very low diffraction
618 angles. In addition to this, these edges correspond to very low system sensitivity

619 (Fig. 6.b), which further decreases the amount of available information in these
620 regions. Tumor detection in these regions would not be reliable for the given
621 position of the system especially at 60 keV.

622 To conclude, the detection of a small tumor situated in regions covered
623 also by another hole than the first one is optimum (in terms of dose received)
624 with a 60 kVp incident spectrum, for the considered system. This detection
625 corresponds to a binary task, presence or absence of a tumor, where it is not
626 necessary to identify the different tissue types present in each sample voxel.
627 Reconstruction of an image slice is more complex task. Here, we require spatial
628 information concerning each tissue type everywhere in the sample. In this case,
629 energies higher than 60 keV provide useful information for regions imaged with
630 low scattering angles. If the collimation system was conceived in a way that
631 edge regions were also covered by other holes, i.e. higher scattering angles, edge
632 artifacts might be avoided even with an incident spectrum at 60 kVp.

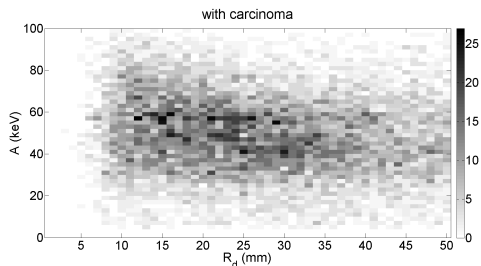


Figure 11: Example of a simulated XRD spectrum with a tumor at its center for scan position $x = 0$ (center in x,y -plane): 30 mm thick fibroglandular region, 100 kVp incident spectrum, $5 \cdot 10^6$ incident photons.

633 5. Conclusion

634 The present study indicates that coherent scattering of X-rays appears as a
635 very promising technique to classify breast tissues when classical mammography
636 gives an unclear result, and to reduce the number of unnecessary breast biopsies.

637 We dimensioned an XRD system, in particular the secondary collimation
638 (hole size, collimation height, number of holes, sensitivity distribution), com-

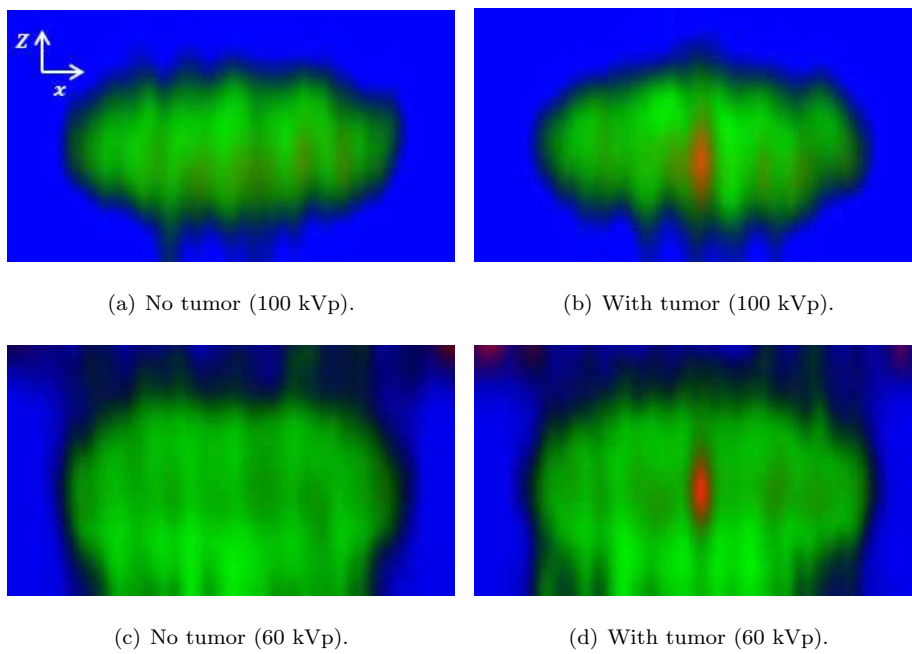


Figure 12: Reconstructed images for incident spectra with 100 keV or 60 keV maximum energy (blue = adipose tissue, green = fibroglandular tissue, red = carcinoma, black = blue+green).

639 binning EDXRD information at different scattering angles, for use as a second
640 control after conventional mammography. In this article, we evaluated its per-
641 formance in breast imaging in terms of separation power. Therefore, XRD
642 spectra for phantoms with and without tumor were used and the required dose
643 to distinguish between these two kinds of spectra was calculated.

644 It was found that the sensitivity and specificity of the method were good
645 even when the dose delivered was moderate. To achieve a 3σ separation, a
646 dose around 0.3 mGy is needed if the tumor is situated in the center of the
647 breast. This dose is very acceptable compared to conventional mammography
648 (1-3 mGy). When the tumor was not in the center of the breast, the required
649 dose increased slightly, but remained very low provided the tumor was located
650 within the field of sensitivity.

651 Delivered dose is also impacted by the choice of the incident X-ray spectrum
652 used for imaging. In fact, the number of photons, i.e. the incident dose, nec-
653 essary to detect the tumor depends on the amount of information carried by
654 each detected photon after coherent scattering. This information corresponds
655 to its momentum transfer value, given by the combination of photon energy
656 and its scattering angle. The detected scattering angles are determined by the
657 secondary collimation. Testing of incident tungsten spectra at different tube
658 voltages showed that for the present system the combination of scattering an-
659 gles and photon energies was the best with an incident spectrum at 60 kVp. A
660 system with a different distribution of intercepted scattering angles will have an
661 optimal incident spectrum at a different tube voltage.

662 As the detection of tumors in dense breasts are often a problem in classical
663 mammography, the impact of varying breast density on separation power of the
664 system was tested. It turned out that different breast densities do not affect
665 the detectability of the tumor or the order of magnitude of the required dose.
666 Hence, XRD imaging with the presented system appears to be a well adapted
667 solution at a second control level after conventional mammography. Though,
668 mammography does only allow to identify a suspicious region in the plane and
669 not the exact location of the possible tumor. Therefore, an x,y-scan of this

670 region is required, but scan-time appears to be acceptable. With an incident
671 flux of about $1.5 \cdot 10^8$ photons per cm^2 per mAs at 1 m distance (tube current
672 of about 10 mA), scan-time for 10 cm^3 would be about 2 seconds. A scan slice
673 in x-direction was simulated to assess the imaging qualities of the proposed
674 XRD system. Reconstruction results confirmed that the small tumor can be
675 detected using this system, although spatial resolution was poor compared to
676 other imaging techniques.

677 In future work, it will be necessary to manufacture the XRD system pre-
678 sented here so as to be able to make experimental measurements in order to
679 confirm the simulation results. The impact of variability of breast thickness
680 and tissue scattering signatures should also be studied.

681 References

- 682 [1] P. C. Johns, M. J. Yaffe, X-ray characterisation of normal and neoplastic
683 breast tissues, *Physics in Medicine and Biology* 32 (1987) 675–695.
- 684 [2] S. H. Evans, D. A. Bradley, D. R. Dance, J. E. Bateman, C. H. Jones,
685 Measurement of small-angle photon scattering for some breast tissues and
686 tissue substitute materials, *Physics in Medicine and Biology* 36 (1991) 7–18.
- 687 [3] S. Pani, G. Royle, R. Speller, A. Castoldi, A. Galimberti, C. Guazzoni, Use
688 of a novel controlled drift detector for diffraction enhanced breast imaging,
689 *Nuclear Instruments and Methods in Physics Research Section A: Accel-*
690 *erators, Spectrometers, Detectors and Associated Equipment* 573 (2007)
691 133–136.
- 692 [4] G. J. R. A. Taibi, A Monte Carlo simulation study to investigate the poten-
693 tial of diffraction enhanced breast imaging, *Nuclear Science, IEEE Trans-*
694 *actions on* 3 (2000) 1581 – 1586.
- 695 [5] D. Cunha, A. Tomal, M. Poletti, Diffraction enhanced breast imaging
696 through Monte Carlo simulations, *Nuclear Instruments and Methods in*

- 697 Physics Research Section A: Accelerators, Spectrometers, Detectors and
698 Associated Equipment 652 (2011) 878–882.
- 699 [6] G. Harding, M. Newton, J. Kosanetzky, Energy-dispersive X-ray diffraction
700 tomography, *Physics in Medicine and Biology* 35 (1990) 33–41.
- 701 [7] M. Westmore, A. Fenster, I. Cunningham, Tomographic imaging of
702 the angular-dependent coherent-scatter cross section, *Medical Physics* 24
703 (1997) 3–10.
- 704 [8] J. Griffiths, G. Royle, J. Horrocks, A. Hanby, S. Pani, R. Speller, Angular
705 dispersive diffraction microCT of small breast tissue samples, *Radiation*
706 *Physics and Chemistry* 77 (2008) 373–380.
- 707 [9] S. Pani, E. Cook, J. Horrocks, J. Jones, R. Speller, Characterization of
708 breast tissue using energy-dispersive X-ray diffraction computed tomogra-
709 phy, *Applied Radiation and Isotopes* 68 (2010) 1980–1987.
- 710 [10] G. Kidane, R. D. Speller, G. J. Royle, A. M. Hanby, X-ray scatter signatures
711 for normal and neoplastic breast tissues, *Physics in Medicine and Biology*
712 44 (1999) 1791–1802.
- 713 [11] M. J. Farquharson, K. Geraki, The use of combined trace element XRF
714 and EDXRD data as a histopathology tool using a multivariate analysis
715 approach in characterizing breast tissue, *X-Ray Spectrometry* 33 (2004)
716 240–245.
- 717 [12] R. J. LeClair, M. M. Boileau, Y. Wang, A semianalytic model to extract
718 differential linear scattering coefficients of breast tissue from energy disper-
719 sive x-ray diffraction measurements, *Medical Physics* 33 (2006) 959–967.
- 720 [13] A. Chaparian, M. Oghabian, V. Changizi, M. Farquharson, The optimiza-
721 tion of an energy-dispersive X-ray diffraction system for potential clinical
722 application, *Applied Radiation and Isotopes* 68 (2010) 2237–2245.

- 723 [14] M. A. O. Ali Chaparian, Introducing an Optimized Method for Obtaining
724 X-ray Diffraction Patterns of Biological Tissues, *Iranian Journal of Medical*
725 *Sciences* 8 (2012) 9–17.
- 726 [15] B. Ghammraoui, L. M. Popescu, A. Badal, Monte carlo evaluation of the
727 relationship between absorbed dose and contrast-to-noise ratio in coherent
728 scatter breast CT, in: *Proc. SPIE 9412, Medical Imaging 2015*, 2015.
- 729 [16] B. Ghammraoui, A. Badal, L. M. Popescu, Maximum-likelihood estima-
730 tion of scatter components algorithm for x-ray coherent scatter computed
731 tomography of the breast, *Physics in Medicine and Biology* 61 (2016) 3164–
732 3179.
- 733 [17] C. Malden, R. Speller, Cdznite array for the detection of explosives in bag-
734 gage by energy-dispersive X-ray diffraction signatures at multiple scatter
735 angles, *Nuclear Instruments and Methods in Physics Research, Section*
736 *A: Accelerators, Spectrometers, Detectors and Associated Equipment* 449
737 (2000) 408–415.
- 738 [18] D. O’Flynn, C. B. Reid, C. Christodoulou, M. D. Wilson, M. C. Veale,
739 P. Seller, D. Hills, H. Desai, B. Wong, R. Speller, Explosive detection using
740 pixellated X-ray diffraction (PixD), *Journal of Instrumentation* 8 (2013)
741 P03007.
- 742 [19] F. Marticke, C. Paulus, G. Montémont, O. Michel, J. I. Mars, L. Verger,
743 Multi-angle reconstruction of energy dispersive X-ray diffraction spectra.,
744 in: *Workshop on Hyperspectral Image and Signal Processing: Evolution in*
745 *Remote Sensing (IEEE)*, 2014.
- 746 [20] J. A. Griffiths, G. J. Royle, A. M. Hanby, J. A. Horrocks, S. E. Bohndiek,
747 R. D. Speller, Correlation of energy dispersive diffraction signatures and
748 microCT of small breast tissue samples with pathological analysis, *Physics*
749 *in Medicine and Biology* 52 (2007) 6151–6164.

- 750 [21] E. Ryan, M. Farquharson, Breast tissue classification using x-ray scatter-
751 ing measurements and multivariate data analysis, *Physics in Medicine and*
752 *Biology* 52 (2007) 6679–6696.
- 753 [22] M. E. Poletti, O. D. Goncalves, I. Mazzaro, X-ray scattering from human
754 breast tissues and breast-equivalent materials, *Physics in Medicine and*
755 *Biology* 47 (2002) 47.
- 756 [23] C. R. F. Castro, R. C. Barroso, M. J. Anjos, R. T. Lopes, D. Braz, Coherent
757 scattering characteristics of normal and pathological breast human tissues,
758 *Radiation Physics and Chemistry* 71 (2004) 649–651.
- 759 [24] O. R. Oliveira, A. L. C. Conceição, D. M. Cunha, M. E. Poletti, C. A. Pelá,
760 Identification of Neoplasias of Breast Tissues Using a Powder Diffractome-
761 ter, *Journal of Radiation Research* 49 (2008) 527–532.
- 762 [25] A. Conceio, M. Antoniassi, M. Poletti, L. Caldas, Preliminary study of
763 human breast tissue using synchrotron radiation combining WAXS and
764 SAXS techniques, *Applied Radiation and Isotopes* 68 (2010) 799–803.
- 765 [26] D. L. Batchelar, Bone-composition imaging using coherent-scatter com-
766 puted tomography: Assessing bone health beyond bone mineral density,
767 *Medical Physics* 33 (2006) 904–915.
- 768 [27] G. Poludniowski, G. Landry, F. DeBlois, P. M. Evans, F. Verhaegen,
769 SpekCalc: a program to calculate photon spectra from tungsten anode
770 x-ray tubes, *Physics in Medicine and Biology* 54 (2009) N433.
- 771 [28] J. S. Francesc Salvat, Jos M. Fernndez-Varea, PENELOPE-2008: A Code
772 System for Monte Carlo Simulation of Electron and Photon Transport,
773 OECD, 2008.
- 774 [29] F. A. Duck, *Physical Properties of Tissue: A Comprehensive Reference*
775 *Book*, Academic Press, 1990.

- 776 [30] G. Harding, B. Schreiber, Coherent X-ray scatter imaging and its applica-
777 tion in biomedical science and industry, *Radiation Physics and Chemistry*
778 56 (1999) 229–245.
- 779 [31] J. Greenberg, K. Krishnamurthy, D. Brady, Snapshot molecular imaging
780 using coded energy-sensitive detection, *Optics Express* 21 (2013) 25480–
781 25491.
- 782 [32] M. N. Lakshmanan, R. E. Morris, J. A. Greenberg, E. Samei, A. J. Kapa-
783 dia, Coded aperture coherent scatter imaging for breast cancer detection:
784 a Monte Carlo evaluation, in: *Proc. SPIE 9783, Medical Imaging 2016:*
785 *Physics of Medical Imaging*, 2016.
- 786 [33] G. Montemont, S. Lux, O. Monnet, S. Stanchina, L. Verger, Studying Spa-
787 tial Resolution of CZT Detectors Using Sub-Pixel Positioning for SPECT,
788 *IEEE Transactions on Nuclear Science* 61 (2014) 2559–2566.
- 789 [34] A. Michalowska, O. Gevin, O. Lemaire, F. Lugiez, P. Baron, H. Grabas,
790 F. Pinsard, O. Limousin, E. Delagnes, IDeF-X HD: A low power multi-gain
791 CMOS ASIC for the readout of Cd(Zn)Te detectors, in: *2010 IEEE Nuclear*
792 *Science Symposium Conference Record (NSS/MIC)*, 2010.
- 793 [35] G. Montemont, M.-C. Gentet, O. Monnet, J. Rustique, L. Verger, Simu-
794 lation and Design of Orthogonal Capacitive Strip CdZnTe Detectors, in:
795 *IEEE Nuclear Science Symposium Conference Record*, 2006, 2006.
- 796 [36] I. A. Cunningham, R. Shaw, Signal-to-noise optimization of medical imag-
797 ing systems, *Journal of the Optical Society of America A, Optics and Image*
798 *Science* 16 (1999) 621–632.
- 799 [37] S. ke Starck, M. Bth, S. Carlsson, The use of detective quantum efficiency
800 (DQE) in evaluating the performance of gamma camera systems, *Physics*
801 *in Medicine and Biology* 50 (2005) 1601–1609.

- 802 [38] J. A. Greenberg, M. N. Lakshmanan, D. J. Brady, A. J. Kapadia, Opti-
803 mization of a coded aperture coherent scatter spectral imaging system for
804 medical imaging, in: Proc. SPIE, 2015.
- 805 [39] D. J. Rhodes, M. K. O'Connor, S. W. Phillips, R. L. Smith, D. A. Collins,
806 Molecular Breast Imaging: A New Technique Using Technetium Tc 99m
807 Scintimammography to Detect Small Tumors of the Breast, Mayo Clinic
808 Proceedings 80 (2005) 24–30.
- 809 [40] M. K. O'Connor, S. W. Phillips, C. B. Hruska, D. J. Rhodes, D. A. Collins,
810 Molecular breast imaging: Advantages and limitations of a scintimammo-
811 graphic technique in patients with small breast tumors, The Breast Journal
812 13 (2007) 3–11.
- 813 [41] L. Shepp, Y. Vardi, Maximum likelihood reconstruction for emission to-
814 mography, IEEE Transactions on Medical Imaging 1 (1982) 113–122.
- 815 [42] F. Marticke, G. Montémont, C. Paulus, O. Michel, J. I. Mars, L. Verger,
816 Calcul analytique de courbes COR en imagerie de diffraction X, in: Gretsi,
817 2015.
- 818 [43] R. A. Parry, S. A. Glaze, B. R. Archer, The aapm/rsna physics tutorial for
819 residents: Typical patient radiation doses in diagnostic radiology, Radio-
820 Graphics 19 (1999) 1289–302.
- 821 [44] D. Hintenlang, Dose measurement in mammography; what are we measur-
822 ing?, in: ACMP Annual Meeting, 2008.
- 823 [45] T. Olgar, T. Kahn, D. Gosch, Average glandular dose in digital mammog-
824 raphy and breast tomosynthesis, RöFo - Fortschritte auf dem Gebiet der
825 Röntgenstrahlen und der bildgebenden Verfahren 184 (2012) 911–918.